

# Discovery and design of high-strength refractory multi-principal element alloys

Prashant Singh,<sup>1,\*</sup> Aayush Sharma,<sup>2</sup> Andrei V. Smirnov,<sup>1</sup> Mouhamad S. Diallo,<sup>2</sup> Pratik Ray,<sup>1,3</sup> Ganesh Balasubramanian,<sup>4</sup> Duane D. Johnson<sup>1,3,\*</sup>

<sup>1</sup>Ames Laboratory, U.S. Department of Energy, Iowa State University, Ames, Iowa 50011 USA

<sup>2</sup>Department of Mechanical Engineering, Iowa State University, Ames, Iowa 50011 USA

<sup>3</sup>Department of Materials Science & Engineering, Iowa State University, Ames, Iowa 50011 USA

<sup>4</sup>Department Mechanical Engineering & Mechanics, Lehigh University, Bethlehem, PA 18015 USA

Keywords: multicomponent alloy, alloy design, high-temperature alloys, linear response, young's modulus

Nickel-based superalloys and near-equiatomic high-entropy alloys (HEAs) containing Molybdenum are known for higher temperature strength and corrosion resistance. Yet, concentrated solid-solution alloys (CSAs) offer a huge design space to tune for optimal properties at slightly reduced entropy. For refractory Mo-W-Ta-Ti-Zr, we showcase KKR electronic-structure methods via coherent-potential approximation (CPA) to identify alloys over 5-dimensional design space with improved mechanical properties and necessary global (formation enthalpy) and local (short-range order) stability. Temperature-dependent deformation is modeled with classical molecular dynamic simulations, validated from our first-principles data. We predict CSAs of improved stability with greatly enhanced strength ( $3\times$  at 300 K) over HEAs, as validated experimentally, and with much improved strength above 500 K over existing commercial alloys ( $2.3\times$  at 2000 K). We also show, due to critical electronic effects, that optimal CSAs are not described well by classical potentials.

Nickel-based superalloys exhibit high-temperature strength, toughness, and oxidation resistance in harsh environments.<sup>1</sup> Improving existing single-crystal alloys is unlikely as melting is near 1653 K, and, heat treatment lowers this to  $\sim 1543$  K. In high-speed turbines, melting reduces below 1523 K at the zone between the bond coat (e.g., NiAl) and the single-crystal blade.<sup>2</sup> As such, the engine efficiency and thrust-to-weight ratio can be improved by a

guided search for new materials. High-entropy alloys (HEAs) based on refractory elements may achieve higher temperature operation with superior creep strength.<sup>3</sup> Typical refractory HEAs exhibit a yield strength of 500 - 700 MPa at 1573K, surpassing Ni-based superalloys.<sup>4</sup> Indeed, at elevated temperatures Mo-based alloys show good thermal (higher conductivities with lower strains<sup>5</sup>) and mechanical (machinability)<sup>6</sup> properties, making them promising candidates.

Almost all HEAs for which mechanical properties have been reported are based on Cr-Fe-Co-Ni with other elements added, e.g., Al,<sup>7</sup> Mn,<sup>8</sup> Mo,<sup>9</sup> and Ti.<sup>10</sup> CoCrFeNi exhibits very high compression strength at 300 K, often exceeding 1500 MPa. Strains in as-cast condition do not often exceed 5-7%, albeit a few exhibit 25-33%.<sup>10,11</sup> Annealing does improve ductility of as-cast alloys.<sup>11</sup> As with conventional alloys, a rapid decrease in strength (i.e., Young's modulus, E) occurs above 0.6 of the melting temperature  $T_m$ , and the strength of alloys approaches 100 MPa at 1273 K.<sup>7</sup>

HEAs consist of  $N(\geq 5)$  elements in near equiatomic compositions ( $c_\alpha \sim 1/N$ ), giving maximal point (mixing) entropy ( $S_{pt} = -\sum_{i=1}^N c_\alpha \ln c_\alpha \xrightarrow{\max} \ln N$ ), that may better form solid solutions due to a compromise between the large  $S_{pt}$  and a formation (mixing) enthalpy  $E_f$  that is not too positive (strongly clustering) nor too negative (strongly ordering).<sup>7</sup> As for binary solid solutions, Hume-Rothery's rules<sup>12</sup> for atomic size difference ( $\delta$ ), crystal structure, valence electron concentration (VEC), and electronegativity difference ( $\Delta\chi$ ) play a similar role in HEA formation. The production of several single or multi-phase alloys with face-centered cubic (FCC or  $A1$ ), body-centered cubic (BCC or  $A2$ ), hexagonal close-packed (HCP or  $A3$ ), or cubic diamond ( $A4$ ) structures exhibiting enhanced high-temperature strength, ductility, fracture and creep resistance to corrosion,<sup>7-10,13,14</sup> and thermal stability<sup>15</sup> validates the concept of HEAs.<sup>7</sup> MoWVNbTa, e.g., with a density of 12.2 g/cm<sup>3</sup>. has a reported usable strength up to 1873 K.<sup>4</sup>

Nonetheless, from an alloy design perspective, concentrated solid-solution alloys (CSAs) offer a huge design space to tune properties, especially considering the strong effects alloying has on electronic properties (“band” filling, hybridization, Fermi-surface nesting, ...), phase stability, and structure. Optimized CSAs offer a slightly reduced entropy with a single-phase region, or two-phase region for enhanced mechanical properties, existing in a desired operational temperature range.<sup>16-18</sup>

Here we narrow the design of high-strength, refractory Mo-W-Ta-Ti-Zr alloys via KKR electronic-structure methods within density-functional theory (DFT) using the coherent-potential approximation (CPA) to handle chemical disorder and thermodynamic averaging,<sup>16,17</sup> as reported in 3d CSAs.<sup>18,19</sup> The well-established KKR-CPA predicts structural properties, elastic moduli, and phase stability versus compositions  $\{c_\alpha\}$ , and short-range order (SRO) via thermodynamic linear response,<sup>18,20-23</sup> a method, in particular, which revealed the origin for Hume-Rothery’s size-effect rule.<sup>21,24</sup> Notably, global stability ( $E_f$ ) and local instability (SRO) should be jointly assessed: While segregation is expected for  $E_f > 0$ , SRO can be segregating from local compositional instabilities even if  $E_f < 0$ . To rapidly predict mechanical behavior (e.g.,  $E$ ) versus temperature ( $T$ ), we performed extensive molecular dynamics (MD) simulations based on semi-empirical potentials, validated in part by first-principles results (and also highlighting limitations of such methods). The tuned and proposed refractory quinary alloys and their properties are placed in context to Hume-Rothery-type design targets and compared to experiments.

## **I. HUME-ROTHERY DESIGN TARGETS:**

HEAs contain elements with  $c_\alpha \sim 35-12$  at.% ( $N=3-8$ ). Trial-and-error has led to alloys with simple crystal structures, and a few with extraordinary properties,<sup>25</sup> e.g., formability using size disparate elements for con- fusion by design.<sup>26</sup> For CSAs design of phase stability and of

electronic and mechanical behavior, targets for DFT-based KKR-CPA are limited by extending Hume-Rothery<sup>12</sup> (HR) criteria:

1. **Size:** Solute and host atomic radii (in elemental solid) must differ by < 15%.<sup>12,21</sup> For CSAs, with  $\bar{r} = \sum_{i=1}^n c_i r_i$ , size limit in terms of standard deviation is sensible:  $0 \leq \delta \leq 6\%$ , with  $\delta = 100\% \times [\sum_{i=1}^n c_i (r_i^2 - \bar{r}^2) / \bar{r}^2]^{1/2}$
2. **Lattice:** Similar crystal structures for solute and host.
3. **VEC:** Large solubility when solute and host have the same VEC. A metal dissolves one of higher (lower) valency to a greater (lesser) extent.
4.  **$\chi$ 's:** If  $\Delta\chi$  is too great, metals tend to form intermetallic compounds, not solid solutions.
5. **E<sub>f</sub>:** For -11 E<sub>f</sub>+5 mRy CSAs stabilized in usable T's.

A few comments are warranted. In HR1, the 6-6.8% achieves 15%-rule for CSAs with ~50% confidence level, an inequality also found empirically.<sup>27,28</sup> Extending HR3 via electronic density of states concepts, *A2* forms for  $4 < \text{VEC} < 6$  as stability increases when bonding *d*-states fill, and is maximal when half-filled ( $\text{VEC} \approx 6$ ); antibonding states fill with  $\text{VEC} > 6$  (above a pseudogap, see results) and stability decreases. Indeed, *A2* HEAs are observed when VEC is  $5 \pm 1$ .<sup>29</sup> For  $6.8 \leq \text{VEC} \leq 8$  other phases compete, e.g., FeCr has  $\text{VEC} = 7$  (like Mn) and constituent's structure are both *A2*, yet the CSA is unstable to the  $\sigma$ -phase, as often appears.<sup>27</sup> Again, from band filling, *A1* becomes more stable for  $\text{VEC} > 8$ .<sup>30</sup> CSAs are indeed observed to form within these rules.<sup>31</sup> E<sub>f</sub> lower limit in HR5 is set by -T<sub>a</sub>S<sub>pt</sub>, where annealing temperature (needed for kinetics) is T<sub>a</sub> ~ 0.55T<sub>m</sub> (~1000-1650 K for refractories); upper limit is set such that miscibility gap  $T_c^{MG} < T$  (where 158 K ~ 1 mRy). For  $\delta > 5\%$ , HEAs with E<sub>f</sub> > 5 mRy form complex phases, but tend to form metastable metallic glasses for E<sub>f</sub> < -11 mRy.<sup>32</sup> Considering binaries and supercells, these limits for HEA formation are supported.<sup>33</sup> As we have shown, transition temperatures from  $\alpha$  (CSA) to  $\beta$  (ordered or segregated) phases are well estimated from calculated E<sub>f</sub>'s;<sup>34,35</sup> For segregating CSAs (E > 0),  $T_c^{MG} \approx E_f / S_{pt}$ ,<sup>34</sup> and, for ordering CSAs with  $\Delta E_f^{\alpha \rightarrow \beta} = E_f^\alpha - E_f^\beta > 0$ , the order-disorder transition is  $T_c^{od} \approx \Delta E_f^{\alpha \rightarrow \beta}$ .<sup>35</sup> Notably, HR4 also reveals if vibrations are important, as vibrational entropy in binaries correlates as  $\Delta S_{vib} = -\Delta\chi/3 (\pm 0.06 \Delta\chi)$ .<sup>36</sup> Thus, we may quickly estimate T<sub>c</sub> for *d*-band CSAs

as  $T_c^{\alpha \rightarrow \beta} \approx T_{c,pt}^{\alpha \rightarrow \beta} [1 + \Delta S_{vib}^{\alpha \rightarrow \beta} / \Delta S_{c,pt}^{\alpha \rightarrow \beta}]^{-1}$ , which reproduces measured trends without phonon calculations.<sup>34</sup> These estimates are within 5 - 10%.<sup>34,35</sup>

## II. RESULTS IN Mo-W-Ta-Ti-Zr

As a predictive guide, we use KKR-CPA results to tune ( $E_f$ ,  $\delta$ , VEC, and  $\Delta\chi$ ) versus  $\{c_\alpha\}$  to find Mo-W-Ta-Ti-Zr alloys in 5D space with better stability and mechanical properties. Results identify the stability of competing phases, possible multiphase regions, electronic properties, and practical design limits. We use the above criteria to restrict search space for mechanical simulations.

Here, via the KKR-CPA, we search all CSAs without restrictions on  $\{c_\alpha\}$ , or the need for large supercells, as  $A1, A2$  ( $A3$ ) have only 1 (2) atoms per cell. In this quinary, atomic size of Zr (1.60 Å) is largest, followed by Ti, Ta, and W, Mo (1.46, 1.43, and 1.37, 1.36 Å), where bandwidths (inversely related to atomic size) and alloy hybridization determine the effect of size.<sup>21</sup> For  $\chi$  (or  $\Delta\chi$ 's), reflecting solubility and vibrational entropy,<sup>34,36</sup> (W, Mo) have largest  $\chi$  (2.36, 2.16), followed by (Ti, Ta, Zr) with (1.54, 1.50, 1.33). From  $\Delta\chi$  (Mo, W) would have the largest solubility (mixing) range, while %Zr is smaller based on  $\delta$ . Larger %W increases Young's modulus for engineering needs, but increases weight, and %Zr reduces Ti content while positively impacting flow stress.<sup>37</sup>

**Design & Assessment:** For Mo-W-Ta-Ti-Zr, results are most easily presented in a cut through 5D  $\{c_\alpha\}$  space to visualize with only two parameters ( $x, y$ ) along lines or planes (Fig. 1), changing  $\{c_\alpha\}$  in obvious ways. First, we exemplify (see supplement Fig. S1) our accuracy for  $E_f$  vs.  $x$  in  $Ta_{1-x}W_x$ , which agrees well with measured values (within 5%), and ordering enthalpies are low (<310 K) compared to melting. For  $Mo_x(TiZrTaW)_{1-x}$ , we find that  $A2$  is favored over  $A1$  or  $A3$ , and that increasing %Mo (larger  $x$ ) helps stabilize  $A2$ , but  $E_f$  stays positive, so the system segregates albeit more weakly. For  $x=0.4$ ,  $A4$  phase competes

with  $A2$ , and Frank-Kasper phases, like  $C15$ - $\text{Mo}_2(\text{Ti-Zr})$ , may be anticipated. Elements are added to stabilize or change, e.g., oxidation resistance. By adding Al, we see that it acts as an  $A2$  stabilizer up to 20%Mo, as in  $\text{CrFeCoNi-Al}$ .<sup>19</sup> however, adding 5%Si destabilizes  $A2$  relative to Al. So, we focus on  $A2$  Mo-W-Ta-Ti-Zr.

We now assess CSAs that best satisfy design criteria, and local stability. Along with other targets, KKR-CPA  $E_f$  vs.  $\{c_\alpha\}$  for  $(\text{Mo-W})_x\text{Ta}_y(\text{Ti-Zr})_{1-x-y}$  are shown in Fig. 1. Clearly,  $E_f$  for equiatomic case is too positive (+12.7 mRy), and decomposition is expected (with  $T_c^{MG}=1244$  K from estimates in HR section) and confirmed below via SRO (Fig. 3) with spinodal  $T_{sp}=1240$  K. Also, the predicted segregation is corroborated by our experiments, see supplement Fig. S6. To visualize key alloying effects for these CSAs, we plot in Fig. 2 the electronic dispersion and projected total density of states (TDOS), referenced to each alloy's Fermi energy,  $\varepsilon_F$ . With disorder, dispersion exhibits broadening in E and k, showing that k is a "good" (on the scale of the Brillouin zone) but not an exact quantum number (as for zero-width, ordered bands); the width  $dk \sim l_e^{-1}$  ( $l_e$  is the electron scattering length) and gives rise to increased residual resistivity, as may be calculated.<sup>38</sup>

Guided by such details, we can improve CSA properties. The equiatomic alloy has a TDOS with  $\varepsilon_F$  not yet in the pseudogap between bonding and antibonding states (top Fig. 2), so this alloy does not satisfy the design criteria. By integrating states from  $\varepsilon_F$  to the pseudogap, 0.2 electrons are needed to fill bonding states and improved stability. More at.%Mo-W (VEC=6) adds electrons, moving  $\varepsilon_F$  up (Fig. 2), and  $E_f$  decreases better stabilizing CSAs (Fig. 1). Some %Ta is necessary to alter states near  $\varepsilon_F$ : the flat bands near  $\Gamma$  in Fig. 2 are removed from  $\varepsilon_F$  for C7, lowering  $E_f$ , and SRO changes from clustering in C6 to ordering in C7, while  $E \sim 0$ . Here,  $E_f$  reduces quickly for MoW with a small %Ta and %TiZr, while K increases quickly (inset Fig. 1). Notably, the dispersion of  $A2$  elemental metals is canonical when scaled by

bandwidth (inverse atomic size), and so the behavior of the alloy dispersion is fairly generic and predominantly determined by relative composition and size, hybridization, and band filling.

To promote oxide-scale formation for protection, and light weighting, Al is often added. In Fig. 2, 5%Al added at the expense of Ta to C6 (whose  $E_f=+0.70$  mRy) increases disorder broadening (from Al *sp-d* hybridization) and causes d-state around  $\Gamma$  (predominantly TiZr) to again straddle  $\epsilon_F$ . This Fermi surface feature makes  $E_f$  much more positive (+6.8 mRy, with  $T_c^{MG}=828$  K) and the SRO shows stronger clustering with  $T_{sp}=780$  K (see supplement Fig. S5), with Al-Mo pairs most significant, suggesting that Al will segregate to surfaces due its faster kinetics, as needed for oxide formation. Hence, adding Al at the expense of Ta or TiZr, which decreases VEC and drops  $\epsilon_F$  into flat *d*-states, reduces stability; so a balance must be struck by keeping some Ta and TiZr and making VEC high enough to be near  $E_f \sim 0$  and large bulk moduli  $K$  (Fig. 1). Unlike in other systems, Al is not generically a good *A2* stabilizer, as it leads to larger electron scattering for reduced stability, increased resistivity, and decreased thermal transport, see [18] and references therein.

**Chemical SRO:** From KKR-CPA linear response (see Methods), we predict (Fig. 3) Warren-Cowley atomic pair correlations  $\alpha_{\mu\nu}(k;T)$ , whose largest peak at wavevector  $k_0$  reveals the unstable (Fourier) modes to ordering, or clustering at  $\Gamma=(000)$ . As an alloying guide, SRO identifies pairs driving the instability, and predicts the spinodal  $T_{sp}$ , where  $\alpha_{\mu\nu}^{-1}(k_0; T_{sp})=0$  signifying the absolute instability to this chemical fluctuation.<sup>18,19</sup> In real-space, pair probabilities are  $P_{ij}^{\mu\nu}=c_\mu^i c_\nu^j (1 - \alpha_{\mu\nu}^{ij})$ , with  $\alpha_{\mu\nu}^{i \neq j} = 0$  for no SRO, and  $\alpha < 0$  ( $\alpha > 0$ ) indicates ordering (clustering) with bounds of  $-\frac{1}{[\min(c_\mu, c_\nu)]^2} \leq \alpha_{\mu\nu}^{i \neq j} \leq 1$ .

Near equiatomic alloys have maximal SRO peaks in  $\alpha_{\mu\nu}(k_0=\Gamma; T>T_{sp})$ , Fig. 3, signaling in specified pairs spinodal (infinite wavelength) decomposition at  $T_{sp}$  of 1240 K for C1, and at

500 K for C6. This 60% drop in  $T_{sp}$  is unsurprising given that  $E_f > 0$  and reduces with Mo-W and Ta (Fig. 1). For C7, where  $E_f$  has become negative but small from loss of flat dispersion near  $\Gamma$  at  $\varepsilon_F$ , a weak incommensurate (long-period) ordering is found with SRO peak (Fig. 3) at 70% along N - H at  $k_0 = (0.85, 0.15, 0)$ . This SRO arises from Fermi-surface nesting,<sup>48</sup> with contributions at a radius of  $|k_0| \sim 0.86$ , as confirmed along  $\Gamma$ -H (Fig. 3). [SRO is  $B2$  type if it peaks at  $k_0 = H = \{100\}$ , commensurate with  $A2$  lattice.] For theory and detailed examples, see [18] and [19]. We also show, in Fig. S5, that 5%Al addition to the C6 alloy instigates a clustering instability. The Al-Mo pair drives spinodal decomposition at  $T_{sp}$  of 780 K, which shows the tendency of Al to phase separate from Mo and an indication that Al's clustering tendency might be helpful in promoting stable oxide-layer at high temperatures. These results indicate that alloying may improve oxidation behavior, just as for Fe-Cr with a narrow window for chromia formation. Clearly, KKR-CPA methods address profound electronic and alloying effects not possible from effective potentials, or methods that approximate disorder by ordered configurations.

**Deformation Analysis:** Mechanical properties in HEAs have been studied at macro- and micro-scopic levels,<sup>39,40</sup> but the deformation analysis is the key to establish high-T structural candidates. We perform quasistatic uniaxial loading via MD simulations (see Methods) by deforming the alloy in small but finite steps and equilibrating after each step. For equiatomic case,  $\langle 100 \rangle$  compression (Fig. 4a) reveals a smooth stress- strain curve signaling simple plastic flow. In contrast C3 (0.425at.%Mo) has stress drops and strain-hardening triggered by  $\langle 111 \rangle$  dislocations; a stress drop at 0.065 strain marks the initiation of dislocation with  $A2$  Burgers vector,  $\vec{b} = \frac{1}{2}\langle 111 \rangle$ , from 77 - 2000 K.

Snapshots of the evolution show that dislocations (edge and screw type) triggered these instabilities (Fig. 4b). The defect mobility is affected by local distortions caused by the



different sizes and modulus of the solutes. The rise and drop in stress with increasing strain corresponds to the defect evolution where new dislocations occur after every major stress drop followed by strain-hardening due to dislocation interactions and drag. An investigation of the local structural environment (Fig. 4b) reveals deviation from perfect  $A2$ , as yielding occurs for 300 K. Shear bands (black) are promoted, denoting deformed regions with higher compression. At very high strain the inter-play between edge and screw dislocations can be visualized via the band dynamics (Fig. 4b-4).

For engineering, Young's modulus  $E = 3(1 - 2\nu)K$  is more pertinent than  $K$ , so Poisson's ratio  $\nu$  is key. Small-deformation MD simulations determined  $E$  and  $\nu$  at 300 K, and  $E$  vs.  $T$  was found from the elastic stress-strain curve (Fig. 4a). The KKR-CPA energy versus  $a$  ( $A2$  lattice constants) at  $\{c_\alpha\}$  determines the equilibrium  $a_0$ ,  $E_f$ , and  $K$  (Fig. 4d), all used in Fig. 1.  $E$  versus  $T$  from MD, KKR-CPA (using Grüneisen approximation at low  $T$ ), and experiments are compared in Fig. 4c, including for pure Mo and a commercial Mo-rich "TZM" alloy,<sup>3</sup> which again validate theory results. To confirm our predicted  $E$  in equiatomic C1, we performed indentation measurements on samples prepared by arc-melting (see Methods), and at 300 K we found (Fig. 4c)  $104 \pm 12$  GPa compared to 115 GPa (KKR-CPA) and 120 GPa (MD). As  $K$  changes slowly for binary Mo-W (Fig. 4d), the Poisson effect (variation of  $\nu$ ) controls strength, which requires W- or Mo-rich alloys for larger  $E$  values (Fig. 4d). Similarly, for quinary  $(\text{Mo}_z\text{W}_{1-z})_{0.85}\text{Ta}_{0.10}(\text{TiZr})_{0.05}$ , we find that C10 ( $z = 0.50$ ) has strength similar to C4 (Fig. 4c). Whereas we predict a region around  $\overline{\text{C10}}$  ( $z = 0.05$ , highlighted in Fig. 4d, which is perpendicular to plane in Fig. 1 at C10) shows enhanced stability and moduli, Fig. 4c. For these quinary we find  $3\times$  larger  $E$  than HEAs at 300 K, and alloys like  $\overline{\text{C10}}$  have a much larger, less temperature-dependent modulus (Fig. 4c) above 500 K ( $2.3\times$  at 2000 K) over existing commercial TZM alloys.

Finally, one notable point, albeit not surprising, the classical MD simulations fail to represent

properly the alloys that crossover from  $E_f$  positive to negative (e.g., C4- to-C7 or C3-to-C10) in which electronic dispersion (not addressed by semi-empirical potentials) is controlling the materials physics. Hence, we plot only  $\overline{C10}$  KKR-CPA values in Fig. 4c, as MD values of  $E$  vs.  $T$  for C10 and  $\overline{C10}$  are similar to C4, whereas  $\overline{C10}$  values from first-principles increases over C10, as expected from Fig. 4d.

**Summary** From a design perspective by tuning alloying and electronic structure, concentrated solid-solution alloys (CSAs) generally have superior properties over near-equiatomic alloys, although the design space becomes enormous. Using first-principles KKR-CPA applicable to arbitrary CSAs, we predicted the relative phase stability, dispersion, ordering (including  $T_c$ 's), and mechanical properties over all compositions as a design guide. Using electronic alloy design concepts and criteria, we identified higher strength refractory Mo-W- Ta-Ti-Zr alloys from materials physics and engineering perspectives. Temperature-dependent deformation in selected CSAs was modeled using classical MD simulations, validated from first-principles data, including identifying failures in classical potentials that arose from dispersion effects. We predicted a Mo-rich region of improved stability with enhanced Young's modulus over HEAs (as we confirmed experimentally), and an improved temperature-dependence above 500 K ( $2.3\times$  at 2000 K) over existing commercial alloys. Our electronic-structure approaches and analysis of alloying and stability ( $E_f$ , dispersion, SRO) highlights how instructive these details are in guiding design. The techniques are quite general for assessing any arbitrary multi-principal element solid-solution alloys, where alloying and non-trivial electronic effects play a key role.

## METHODS

**DFT Methods:** KKR electronic-structure is used with the coherent-potential approximation

(CPA) to handle chemical disorder;<sup>16,17</sup> screened-CPA addresses Friedel screening from charge-correlations.<sup>17</sup> Scalar-relativistic effects are included (no spin-orbit). Generalized gradient approximation to exchange-correlation was included through use of libXC libraries.<sup>42</sup> CSAs require only 1-atom (2-atom) cells for  $A1$ ,  $A2$  ( $A3$ ). Brillouin zone (BZ) integrations were performed with Monkhorst-Pack k-point method,<sup>43</sup> with  $12 \times 12 \times 12(6)$  for  $A1$ ,  $A2$  ( $A3$ ) meshes. We used 300 k-points in the irreducible-BZ to visualize dispersion along symmetry lines. Each scatterer's radii were defined by neutral "atoms-in-cell", with interstitial divided proportionally to each scatterer, to improve radial density representation near saddle-points in the electronic density.<sup>44,45</sup> We chose  $L_{\max}=3$  spherical-harmonic basis to include  $s$ ,  $p$ ,  $d$  and  $f$ -orbital symmetries. Shallow core states were included in the valence in all calculations. A variational potential zero  $v_0$  was used to yield kinetic energies nearing those of full-potential methods.<sup>46</sup> For self-consistent densities, complex-energy contour integration<sup>47</sup> used 20-point Gauss-Legendre semicircular contour.

**Chemical SRO:** From KKR-CPA linear-response, we calculate SRO parameters,  $\alpha_{\mu\nu}(\mathbf{k};T)$ , for  $\mu$ - $\nu$  pairs,<sup>18,19</sup> as detailed elsewhere.<sup>20-23,48</sup> Dominant pairs driving SRO are identified from pair-interchange energies,  $S_{\mu\nu}^{(i,j)}(T)$ , or curvature (concentration 2<sup>nd</sup>-variation) of the KKR-CPA grand potential, yielding energy cost for concomitant fluctuations of  $c_{\mu}^i$ ,  $c_{\nu}^j$  at atomic sites  $i$ ,  $j$ .  $S_{\mu\nu}^{(2)}(\mathbf{k}; T)$  reveals the unstable (Fourier) modes with ordering wavevector  $\mathbf{k}_0$  (or clustering at (000)), identifies the origin for phase transitions, and dictates the SRO:  $\alpha_{\mu\nu}^{-1}(\mathbf{k};T) = [c_{\mu}(\delta_{\mu\nu} - c_{\nu})]^{-1}[(\delta_{\mu\nu} c_{\mu}^{-1} + c_{\nu}^{-1}) - (k_B T) S_{\mu\nu}^{(2)}(\mathbf{k}; T)]$ . The spinodal temperature,  $\alpha_{\mu\nu}^{-1}(\mathbf{k}; T) = 0$ , signifies an absolute instability, where to this fluctuation and provides an estimate for  $T_c^{MG}$  or  $T_c^{od}$ .<sup>18,19</sup> For  $N>2$ , pairs driving ordering (clustering) will not necessarily be the same pairs that peak in the SRO due to the matrix inversion that relates them (Fig. 3).

**MD Simulations:** Deformation is evaluated using Large-scale Atomistic/Molecular

Massively Parallel Simulator (LAMMPS) package.<sup>49</sup> The KKR-CPA structural parameters are used to validate potentials for finite-T modeling. The force-field parameters for the quinary are established from available ternary EAM potentials.<sup>50</sup> We verified similar hybrid potential parameter combinatorial technique for HEA, like  $\text{Al}_{0.1}\text{CrCoFeNi}$ .<sup>19</sup> In *A2* lattice, with dimensions  $(30 \times 30 \times 30)a$  (54,000 atoms), we distributed 5 elements via composition to form Mo-W-Ta-Ti-Zr solid solutions. Initially the lattice was melted at 4000 K for 90 ps, followed by a quench to 300 K within 10 ns. Uniaxial deformation was performed after equilibrating and relaxing the structure at high strain, as detailed in supplementary material.<sup>19</sup>

**Synthesis & Characterization:** The equiatomic MoWTaTiZr was synthesized by arc-melting pellets of elemental powder blends (Alfa Aesar, purity  $\geq 99.9\%$ ) in an ultra-high purity argon atmosphere on water-cooled copper hearth. Powders were used to reduce the large macro-segregation that occurs during casting when using elemental chips. With the significant difference in melting temperatures (3695 K for W vs. 1941 K for Ti) a three-step melting process was adopted. Step 1: W and Ta powders were mixed thoroughly in a SPEX 8000 mill, and pressed using a Carver hydraulic press; and the pellet was then arc-melted. Step 2: elemental blends of Mo, Ti and Zr were similarly mixed, pressed and arc-melted. Step 3: both arc-melted buttons were re-melted together for a total of four times to ensure better homogeneity.

Phase analyses were carried out using a Philips PANalytical X-Ray Diffractometer (XRD), in a Bragg- Brentano geometry using  $\text{Cu-K}\alpha$  radiation. Microstructure and phase compositions were analyzed using a FEI Helios NanoLab G3UC Scanning Electron Microscope (SEM), equipped with Oxford Energy Dispersive Spectroscopy (EDS) system. Accelerating voltages of 10-15 kV were employed for imaging and compositional analyses. Compositions were measured at 7 different locations for each phase, with the average composition being presented in Table S1 and x-ray diffraction in Figure S6(a) of the Supplement. The diffraction

pattern indicated the presence of two phases, indexed as a bcc ( $A2$ ) phase with lattice parameter  $3.1713(2)$  Å and a minor phase with  $Fd(-3)m$  space group, like for B32 (NaTi proto- type) or C15 ( $MgCu_2$  prototype) structures, with lattice constant  $7.6148(9)$  Å.

**Nanoindentation:** Nanoindentation utilized a triboindenter HYSITRON TI-900 with a Berkovich ( $3 \mu m$ ) tip. The indenter control module applies a trapezoidal load on the sample for 10sec, followed by 5sec rest, and unloads in 10 sec. To calibrate the sample measurements, which also determine the best-applied load and optimum contact depth, the alloy was scanned (15 measurements) on an arbitrarily chosen sample location to optimize for force vs. displacement. For a minimum of 200 nm of contact depth, a  $6000 \mu N$  load was found to suffice. With these set, we indented the alloy at 30 manually chosen locations to measure the sample's elastic response; for the equiatomic case, the mean values were: Young's modulus of  $103.73 \pm 11.49$  GPa, hardness of  $4.6 \pm 0.34$  GPa, and contact depth of  $231.18 \pm 8.74$  nm.

## ACKNOWLEDGMENTS

Work supported by the U.S. Department of Energy (DOE), Office of Science, Basic Energy Sciences, Materials Science & Engineering Division for theory/code development, and by the Office of Fossil Energy, Cross-cutting Research for application and validation for specific HEAs. Research was performed at Iowa State University and Ames Laboratory, which is operated by ISU for the U.S. DOE under contract DE-AC02-07CH11358. Work by AS, MSD, & GB supported by the Office of Naval Research (grant N00014-16-1-2548), with computing resources from the Department of Defense High-Performance Computing Modernization Program.

## References

- [1] T.M. Pollock, S. Tin, *Journal of Propulsion and Power* **2006**, 22, 361.
- [2] S.J. Balsone, B.P. Bewlay, M.R. Jackson, P.R. Subramanian, J.C. Zhao, A. Chatterjee, T.M. Heffernan, in Proceedings of the International Symposium on Structural Intermetallics, 3rd, Jackson Hole, WY, USA, Sept. 23-27,(2001), pp. 99–108.
- [3] H. Shinno, M. Kitajima, M. Okada, *Journal of Nuclear Materials* **1988**, 155, 290.
- [4] O.N. Senkov, G.B. Wilks, J.M. Scott, D.B. Miracle, *Intermetallics* **2011**, 19, 698.
- [5] S. Shafeie, S. Guo, Q. Hu, H. Fahlquist, P. Erhart, A. Palmqvist, *Journal of Applied Physics* **2015**, 118, 184905.
- [6] J.H. Perepezko, *Science* **2009**, 326, 1068.
- [7] J.-W. Yeh, S.-K. Chen, S.-J. Lin, J.-Y. Gan, T.-S. Chin, T.-T. Shun, C.-H. Tsau, S.-Y. Chang, *Adv. Eng. Mater.* **2004** 6 (5), 299.
- [8] Y.J. Zhou, Y. Zhang, Y.L. Wang, G.L. Chen, *Mater. Sci. Eng. A* **2007**, 454, 260.
- [9] Y.F. Kao, T.J. Chen, S.K. Chen, J.-W. Yeh, *J. Alloys Compd.* **2009**, 488, 57.
- [10] Y.J. Zhou, Y. Zhang, Y.L. Wang, G.L. Chen, *Appl. Phys. Lett.* **2007**, 90, 81904.
- [11] K.B. Zhang, Z.Y. Fu, J.Y. Zhang, J. Shi, W.M. Wang, H. Wang, Y.C. Wang, Q.J. Zhang, *J. Alloys Compd.* **2010** 502, 295.
- [12] W. Hume-Rothery, R.W. Smallman, C.W. Haworth, *The Structure of Metals and Alloys*, The Institute of Metals, London, 1969.
- [13] B. Gludovatz, A. Hohenwarter, D. Catoor, E.H. Chang, E.P. George, R.O. Ritchie, *Science* **2014**, 345, 1153.
- [14] Z. Li, K.G. Pradeep, Y. Deng, D. Raabe, C.C. Tasan, *Nature* **2016**, 534, 227.
- [15] V. Dolique, A.L. Thomann, P. Brault, Y. Tessier, P. Gillon, *Surf. Coat. Technol.* **2010** 204, 1989.
- [16] D.D. Johnson, D.M. Nicholson, F.J. Pinski, B.L. Gyorffy, G.M. Stocks, *Phys. Rev. Lett.* **1986**, 56, 2088.
- [17] D.D. Johnson, F.J. Pinski, *Phys. Rev. B* **1993**, 48, 11553.
- [18] P. Singh, A.V. Smirnov, D.D. Johnson, *Phys. Rev. B* **2015** 91, 224204.
- [19] A. Sharma, P. Singh, P.K. Liaw, D.D. Johnson, G. Bala subramanian, *Sci. Rep.* **2016**, 6, 31028.
- [20] J.B. Staunton, D.D. Johnson, F.J. Pinski, *Phys. Rev. Lett.* **1990**, 65, 1259.
- [21] F.J. Pinski, B. Ginatempo, D.D. Johnson, J.B. Staunton, G.M. Stocks, B.L. Gyorff, *Phys. Rev. Lett.* **1991**, 66, 766.
- [22] J.B. Staunton, D.D. Johnson, F.J. Pinski, *Phys. Rev. B* **1994**, 50, 1450.
- [23] J.D. Althoff, D.D. Johnson, F.J. Pinski, J.B. Staunton, *Phys. Rev. B* **1996**, 50, 1473.
- [24] John Maddox, *News & Views: Making sense of binary alloys*, *Nature* **1991**, 349, 649.
- [25] P.K. Huang, J.-W. Yeh, T.T. Shun, K.K. Chen, *Adv. Eng. Mater.* **2004**, 6, 74.
- [26] A.L. Greer, *Nature* **1993**, 366, 303.

- [27] M.-H. Tsai, J.-W. Yeh, *Mater. Res. Lett.* **2014**, 2,107.
- [28] X. Yang, and Y. Zhang, *Mater Chem. Phys.* **2012**, 132, 233.
- [29] U. Mizutani, *Hume-Rothery Rules for Structurally Complex Alloy Phases*, CRC Press, 2010.
- [30] H.L. Skriver, *The LMTO method*, Springer-Verlag, Berlin, 1984.
- [31] Y. Zhang, T.T. Zuo, Z. Tang, M.C. Gao, K.A. Dahmen, P.K. Liaw, Z.P. Lu, *Progr. Mater. Sci.* **2014**, 1, 61.
- [32] A. Inoue, T. Zhang, T. Masumoto, *J. Non-Crystal. Solids* **1993**, 473, 156.
- [33] M.C. Tropicovsky, J.R. Morris, P.R.C. Kent, A.R. Lupini, G.M. Stocks, *Phys. Rev. X* **2015**, 5, 011041.
- [34] N.A. Zarkevich, T.L. Tan, D.D. Johnson, *Phys. Rev. B* **2007**, 75, 104203.
- [35] A. Alam, B. Kraccek, D.D. Johnson, *Phys. Rev. B* **2010**, 82, 024435.
- [36] O. Delaire, T. Swan-Wood, B. Fultz, *Phys. Rev. Lett.* **2004**, 93, 185704.
- [37] J. Lu, G. Ravichandran, W.L. Johnson, *Acta Materialia* **2003**, 51, 3429.
- [38] W.H. Butler, *Phys. Rev. B* **1985**, 31, 3260.
- [39] A.M. Giwa, P.K. Liaw, K.A. Dahmen, J.R. Greer, *Extreme Mechanics Letters* **2016**, 8, 220.
- [40] Y. Zou, S. Maiti, W. Steurer, R. Spolenak, *Acta Mater* **2014**, 65, 85.
- [41] F.H. Featherston, Thesis, *The Elastic Constants of Tantalum, Tungsten and Molybdenum*, Monterey, California, (1963).
- [42] M.A.L. Marques, M.J.T. Oliveira, T. Burnus, *Comp. Phys. Comm.* **2012**, 183, 2272.
- [43] H.J. Monkhorst, J.D. Pack, *Phys. Rev. B* **1976**, 13, 5188.
- [44] A. Alam, D.D. Johnson, *Phys. Rev. B* **2009**, 80, 125123.
- [45] D.D. Johnson, A.V. Smirnov, S.N. Khan, *MECCA: Multiple-scattering Electronic-structure Calculations for Complex Alloys* (KKR-CPA Program, ver. 2.0), Iowa State University and Ames Laboratory, 2015).
- [46] A. Alam, D.D. Johnson, *Phys. Rev. B* **2012**, 85, 144202.
- [47] D.D. Johnson, F.J. Pinski, G.M. Stocks, *J. Appl. Phys.* **1985**, 57, 3018.
- [48] J.D. Althoff, D.D. Johnson, F.J. Pinski, *Phys. Rev. Lett.* **1995**, 74, 138.
- [49] S. Plimpton, *J. Comp. Phys.* **1995**, 117, 1.
- [50] X.W. Zhou, R.A. Johnson, H.N.G. Wadley, *Phys. Rev. B* **2004**, 69, 144113.

**Figure 1.**(Color online)  $E_f$  and  $K$  (inset) vs.  $(x,y)$  for  $(\text{MoW})_x\text{Ta}_y(\text{TiZr})_{1-x-y}$ , a cut through 5D  $\{c_a\}$  space containing equiatomic composition (C1), and plotted with vertical (dashed) lines of constant VEC (4-6) and contours of constant  $\delta$  (1-6). Besides global stability ( $E_f$ ), alloys exhibit local instability (SRO) to segregation (tri-angles) or ordering (circles). DFT results are every 5% and interpolated. Maximal  $K$  is near C7-10 with  $\sim 300$  GPa, where  $E_f \sim 0$  and segregation is lost (Fig. 3).

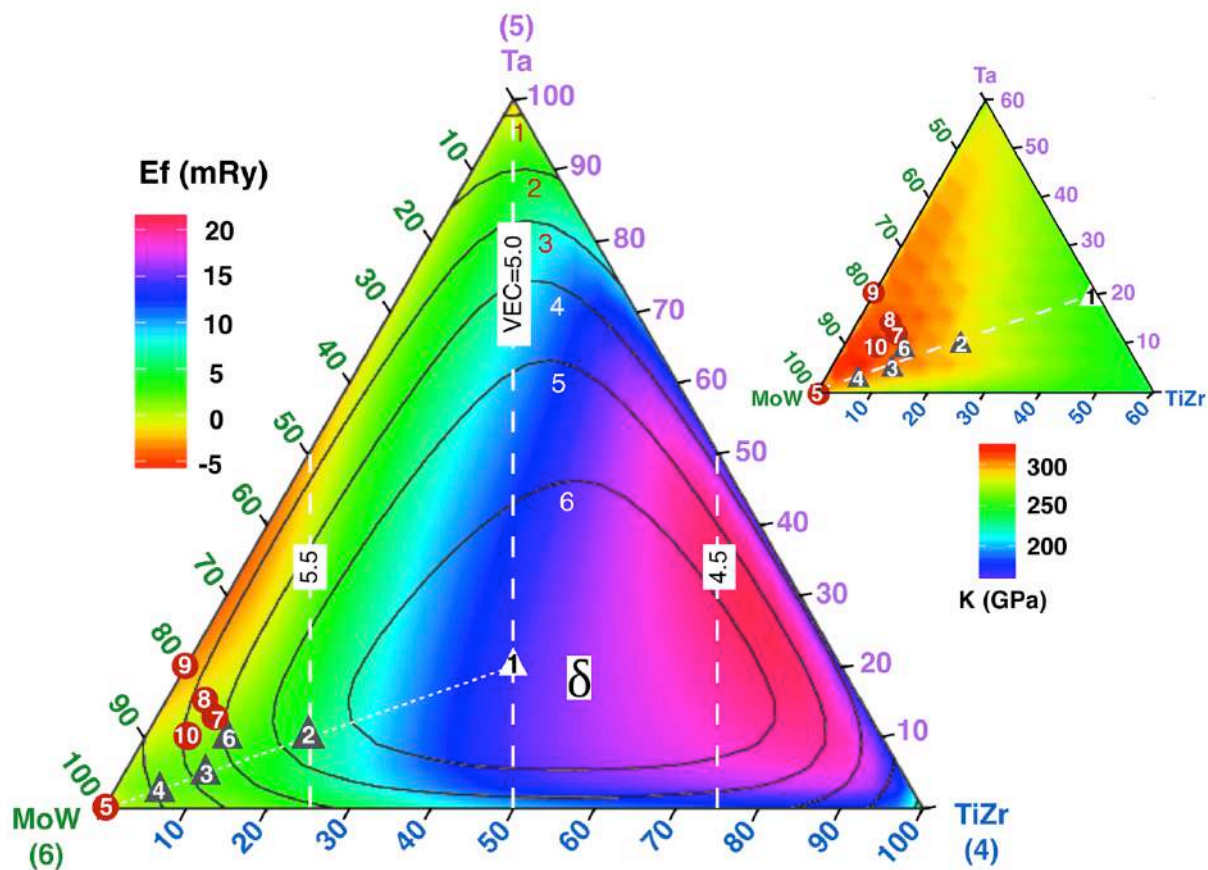




**Figure 2.** (Color online) For C1, C6, C7 in Fig. 1, the electronic dispersion along Brillouin Zone high-symmetry lines, and the projected total density of states (TDOS). Effects of Al doping is also shown (bottom). By tuning  $\{c_\alpha\}$  to add electrons, shift dispersion, or change disorder, the pseudogap is reached near  $\epsilon_F$  (0), better stabilizing the alloy and altering segregation.

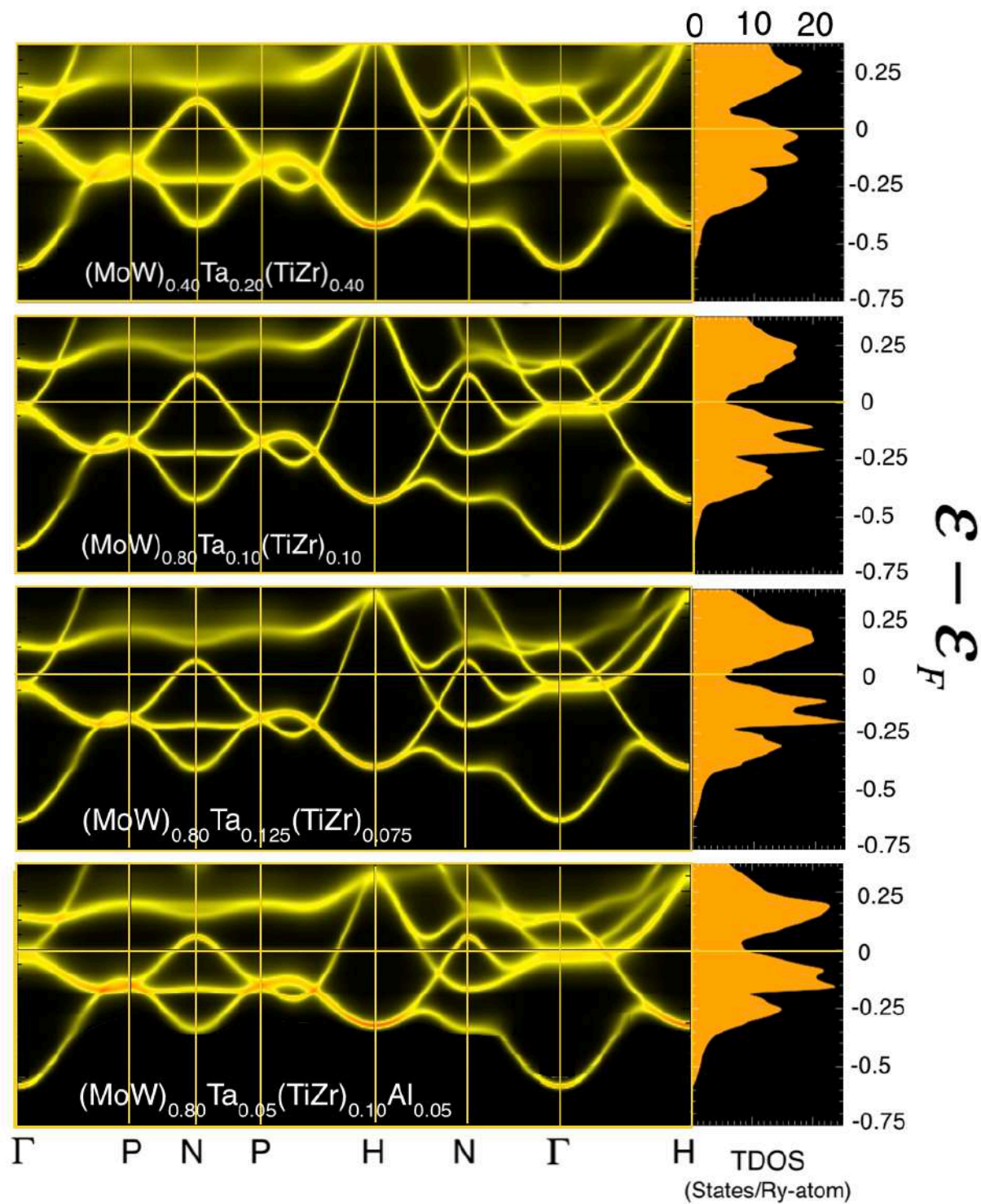


**Figure 3.** (Color online) For three alloys in Fig. 1, SRO correlations (top)  $\alpha_{\mu\nu}(\mathbf{k}; 1.15T_{\text{sp}})$  and (bottom) energies  $S_{\mu\nu}^{(2)}(\mathbf{k}; 1.15T_{\text{sp}})$  plotted along high-symmetry lines in the Brillouin zone: (left) C1 ( $x=2/5, y=x/2$ ) with  $\alpha_{\text{TiZr}}(\Gamma)$  clustering with  $T_{\text{sp}}=1240$  K; (middle) C6 ( $x=4/5, y=1/10$ ) with  $\alpha_{\text{ZrMo}}(\Gamma)$  clustering with  $T_{\text{sp}}=500$  K; and (right) C7 ( $x=4/5, y=1/8$ ) with  $\alpha_{\text{TiMo}}(\mathbf{k}_0)$  with incommensurate ordering  $|\mathbf{k}_0| = 0.7|\mathbf{N}-\mathbf{H}|$  with  $T_{\text{sp}}=298$  K. For C1 [C6], Ti-Zr [Zr-Mo] pairs dominate correlations, but clustering is driven by  $S_{\mu\nu}^{(2)}(\Gamma)$ . In C7, Ti-Mo dominate correlations, but Ti-Mo and Ta-W drive ordering.

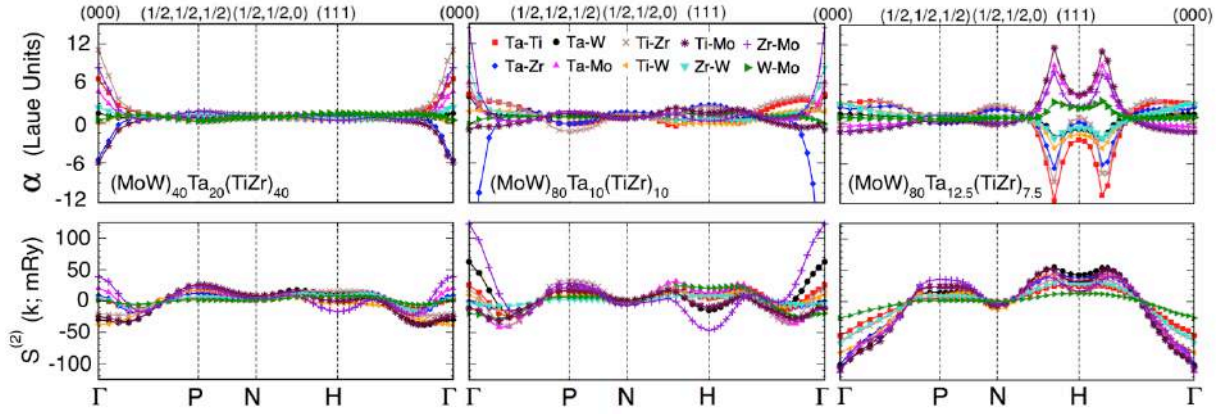
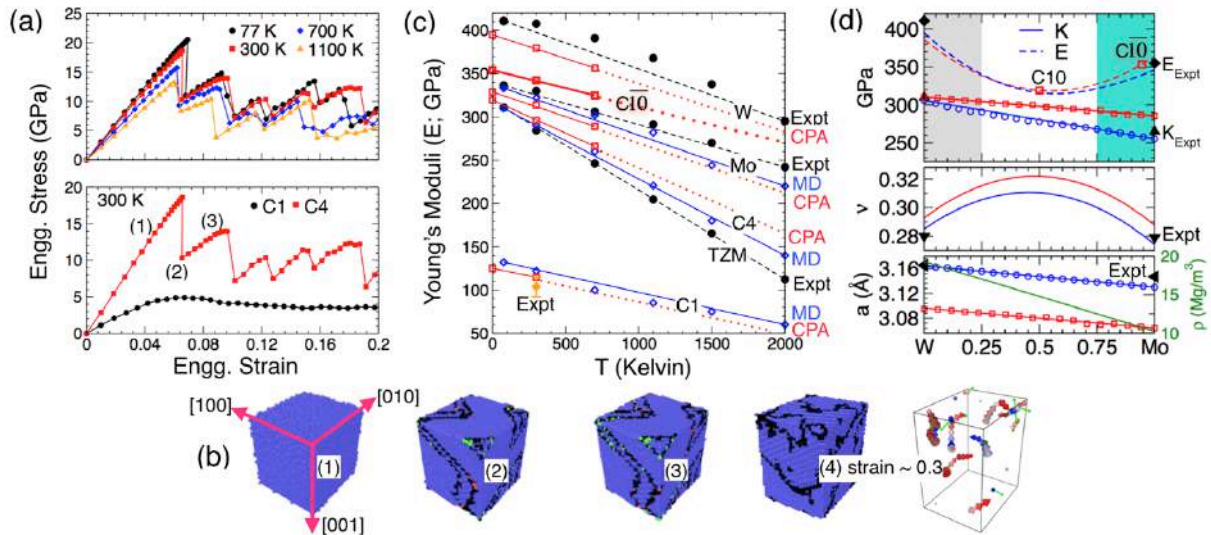


**Figure 4.** (Color online) (a, bottom) Simulated stress-strain for uniaxial quasi-static compression at 300 K for equiatomic C1 alloy, which exhibits simple plastic flow, and for C4 alloy, also versus T (a, top) from 77 to 1100 K, where stress drops arise from dislocation motion and annihilation. (b) C4 strained elastically to 0.065 (b-1, blue), then, at yield, shear-bands appear (b-2, black) accompanied by dislocations. At high strain-rates ( $\sim 0.3$ ), stronger edge (red) and screw (blue) components are found (b-4) with Burgers vector (green). (c) For (non)equiatomic alloys, E vs. T from classical MD simulations [blue lines and diamonds], first-principles KKR-CPA results [red lines and squares, extended to 600 K via Grüneisen theory, then extrapolated (dotted lines)], and measurements (Expt.) for W, Mo, commercial TZM,<sup>3</sup> and C1 alloy (present experiments). (d) For validation in A2  $\text{Mo}_z\text{W}_{1-z}$ , measured (black symbols) and KKR-CPA results (blue lines and circles) for K,E (GPa), lattice constant  $a$  (Å), and density  $\rho$  ( $\text{Mg/m}^3$ ), with Poisson ratio ( $\nu$ ) from MD. Also, predicted values are shown for quinary  $(\text{Mo}_z\text{W}_{1-z})_{0.85}\text{Ta}_{0.10}(\text{TiZr})_{0.05}$  [red lines and squares], where C10 ( $z=0.5$ ) alloy response is similar to C4 in Fig. 4c. **Proposed design region:** Region around quinary  $z=0.05$  (denoted  $\overline{\text{C10}}$ , at Mo-rich end of a line perpendicular to plane at C10 in Fig. 1) shows enhanced E (above Mo) and better T-dependent slope (Fig. 4c) from a favorable Poisson effect (green area in Fig. 4d). Above 500 K,  $\overline{\text{C10}}$  has larger, less T-dependent E than TZM ( $2.3\times$  at 2000 K).



## Supporting Information

### **Discovery and design of high-strength refractory multi-principal element alloys**

Prashant Singh,<sup>1,\*</sup> Aayush Sharma,<sup>2</sup> Andrei V. Smirnov,<sup>1</sup> Mouhamad S. Diallo,<sup>2</sup>  
Pratik Ray,<sup>1,3</sup> Ganesh Balasubramanian,<sup>4</sup> Duane D. Johnson<sup>1,3,\*</sup>

Below we provide the supporting material referenced in the test, as well as other results that help support the paper and its methodologies.

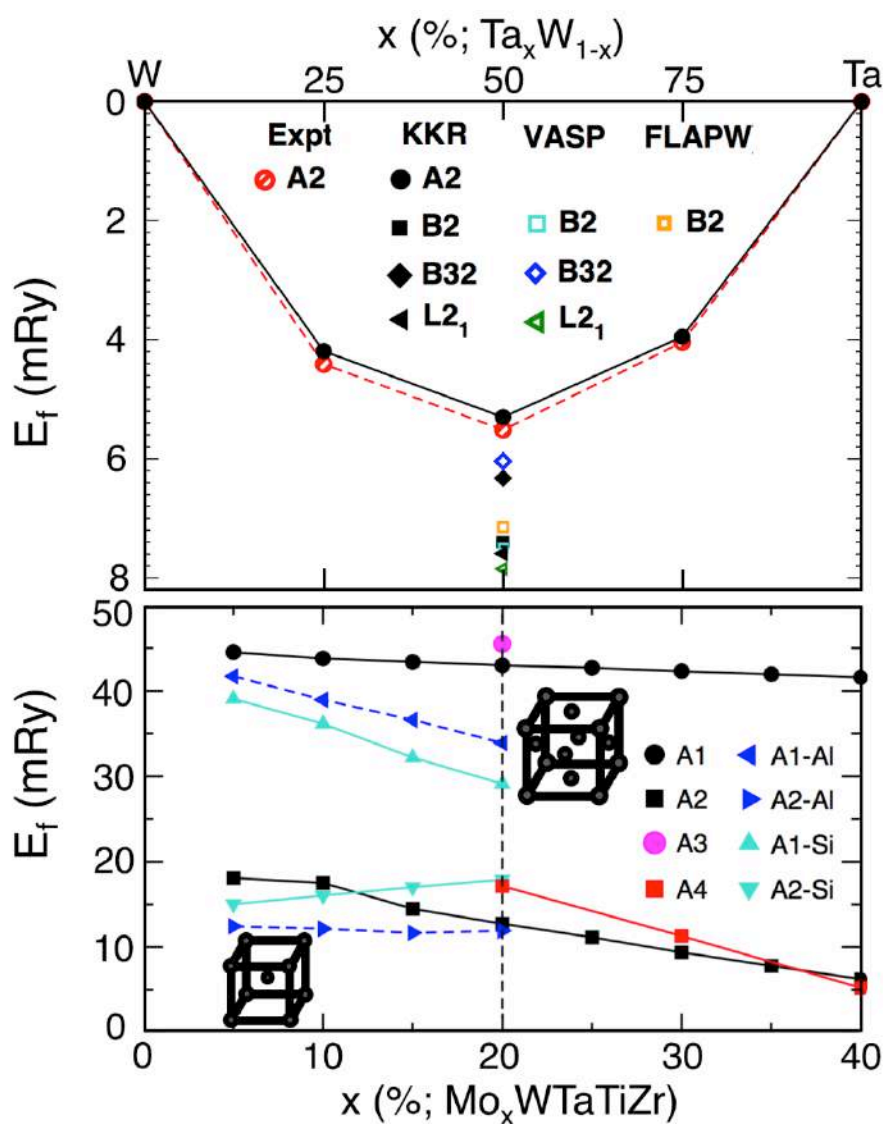
We use *ab initio* Korringa-Kohn-Rostoker coherent-potential-approximation (KKR-CPA) method to characterize the effects of chemical disorder on the electronic and structural properties of solid-solution alloys. The KKR-CPA is mathematically formulated to calculate the configurationally-averaged lattice constants, formation enthalpy, and electronic structure, including total densities of states and dispersion within a single-site, mean-field theory.<sup>1-5</sup> Moreover, as with standard band-structure methods, the KKR-CPA can calculate many other configurationally-averaged properties, e.g., bulk-modulus, resistivity and susceptibilities via linear-response.<sup>1-7</sup> Notably, it is the configurationally-averaged properties of random solid solutions that are measured by experiments, such as diffraction and spectroscopy.

#### **Criteria of phase selection:**

In Figure S1, we assess the accuracy for our KKR-CPA formation energies,  $E_f$ , and identify competing structures. We exemplify  $E_f$  vs.  $x$  for  $W_{1-x}Ta_x$  (top-panel), showing  $A2$  results agree well with experiment (within 5%). Also, we show results for specific ordered cells, which are compared to and agree well with other reliable band-structure methods [VASP pseudo-potential<sup>8</sup> and full-potential linear-augmented plane-wave (FLAPW)<sup>9</sup>]. For  $(TiZrTaW)_{1-x}Mo_x$  (bottom-panel) we show that  $A2$  is favored over  $A1$  or  $A3$  (with  $a$  and  $c/a$

optimized). As such, a is reasonable, we focus mainly on  $A2$ -phase of the alloy in the main text. Increasing %Mo (larger  $x$ ) helps stabilize  $A2$ , but  $E_f$  stays positive, so the system segregates but more weakly.

**Figure S1.** (Color online) (Top) Calculated formation energies ( $E_f$ ) for  $Ta_xW_{1-x}$  agree well with measured values. (Bottom) For  $(TiZrTaW)_{1-x}Mo_x$ , ( $E_f$ ) versus  $x$  showing relative stability of  $A1$ ,  $A2$ , and  $A3$  phases. While  $A2$  is most favored, positive  $E_f$  indicates segregation tendency, so  $E_f \approx 0$  stabilizes the  $A2$  phase.



### **Lattice Constants (*a*) for High-throughput Assessments:**

Recently, high-throughput computational materials design has become more and more relevant to materials design, in which hundreds of thousands of calculations are subjected to simultaneous testing.<sup>10</sup> The three-step criteria discussed in Ref. [10] is very crucial for efforts, i.e., (a) **Electronic-structure and thermodynamic calculations:** phase and thermodynamic stability;<sup>11,12</sup> (b) **Data storage:** systematic way of storing data;<sup>13</sup> (c) **Data analysis:** Either to select novel materials, or gaining new physical insights, or both.<sup>14-16</sup> For fast screening of Mo-W-Ta-Ti-Zr 5-dimensional composition design space, we used an estimate for lattice constant to perform “high-throughput” calculations to discover the best alloys in terms of phase-stability and/or mechanical behavior, as in text, Fig. 1. Specifically, we estimated alloy lattice constants via Vegard’s rule, which is the concentration-weighted sum of volume optimized elemental lattice constants in the parent alloys (A2) phase, or, simply,  $a_{alloy} = \sum_i [c_i^X a_i^X]$ , where  $i=1, 5$  and  $X= Mo, W, Ta, Ti, Zr$ . With the lattice constants at all compositions estimated (which were within 1-3% for the optimized lattice constants), the entire design space could be calculated (we chose every 5% increments through 5D space) to find regions of interest, as in Fig. 1. With systems of interest identified, we then fully optimized lattice constants to determine formation energies and bulk moduli, as reported, and performed detailed electronic-structure (dispersion and density of states), and thermodynamic linear response (short-range order) for alloy design.

### **Grüneisen correction to lattice constants:**

To estimate lattice constants at low but non-zero temperatures, we used the Grüneisen parameter  $\gamma_0(V)$  from the Dugdale-MacDonald model,<sup>17</sup> and obtain the simple thermal enhancement model

$$\frac{\Delta V}{V_0} = \frac{3\Delta a}{a_0} = \frac{9}{16}(K_1 - 1) \left[ \frac{k_B T}{K_0 V_0} \right]$$

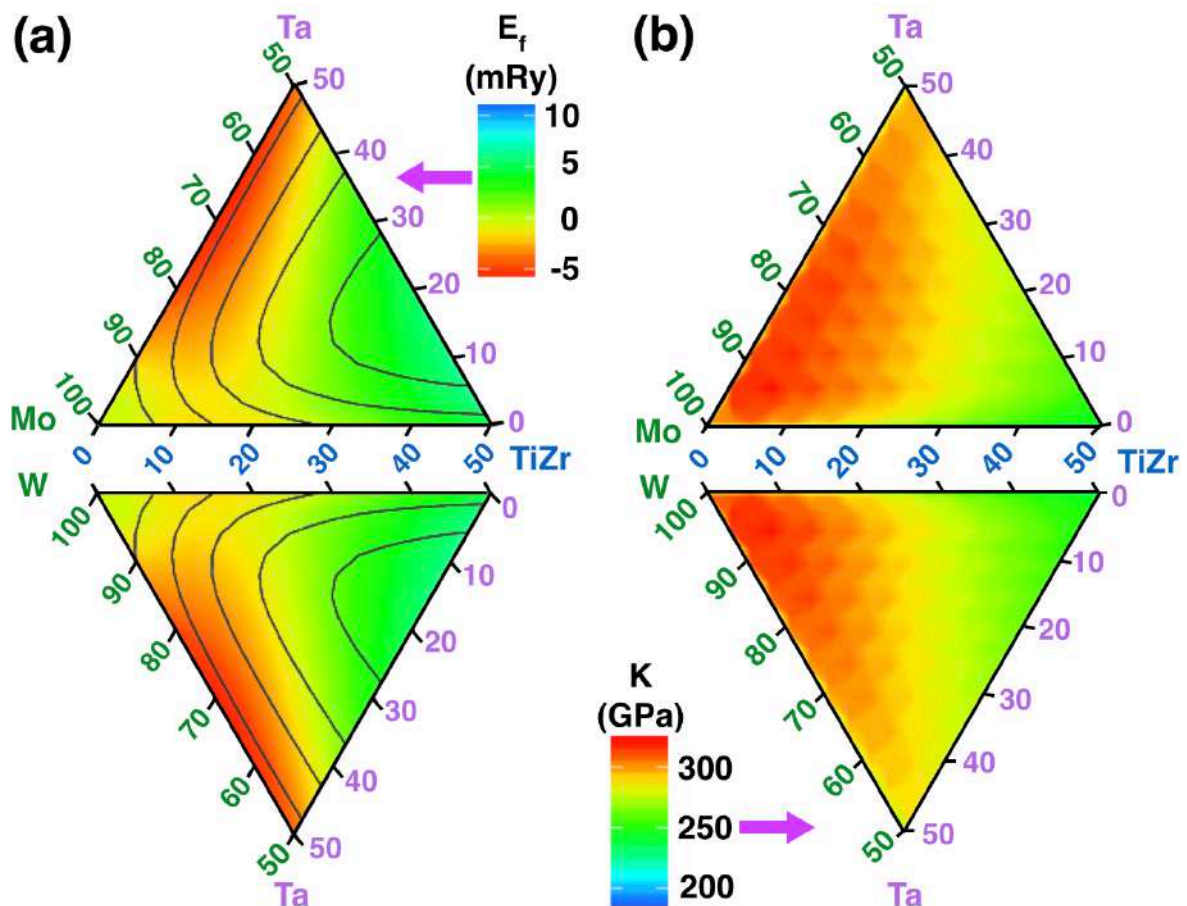
( $K_1$  is the pressure derivative of the bulk modulus at equilibrium lattice constant), Here,  $V_0$  ( $a_0$ ) is equilibrium cubic volume (lattice constant),  $k_B$  is Boltzmann constant,  $K_0$  is bulk modulus at  $a_0$ , and  $T$  is arbitrary (but low) temperature.  $\Delta V$  ( $\Delta a$ ) are volume (lattice) change at non-zero  $T$ . The underlying picture of the Dugdale-MacDonald approximations is valid up to one atom per primitive cell. The approximations may work, but less reliably, when there is more than one atom per cell. The Dugdale-MacDonald model has a correct limit: the anharmonic effects vanish for a harmonic crystal ( $K_1 = 1$ ).<sup>17</sup> Within this model, we estimated the temperature-dependent behavior of lattice constants ( $a$ ) and bulk-modulus ( $K$ ) for each system, see main text, Fig.4(c).



### Phase Stability and Modulus of $X_xTa_y(TiZr)_{1-x-y}$ , $X=Mo(W)$ :

In Figure S2(a) we show  $E_f$  vs.  $(x, y)$  for  $Mo_xTa_y(TiZr)_{1-x-y}$  and  $W_xTa_y(TiZr)_{1-x-y}$  alloys, which are planes at the ends of the  $(MoW)_xTa_y(TiZr)_{1-x-y}$  plane. For comparison to Fig. 1, we plot the bulk modulus ( $K$ ) for the alloys, which shows that adding Mo/MoW/W-rich alloys possess higher strength than Ti/Zr-rich alloys. Hence, along a line perpendicular to C10 in Fig. 1 offers high-strength MoW-rich alloys, which are useful for a variety purposes.<sup>18,19</sup>

**Figure S2.** (Color online) Similar to Fig. 1, (a)  $E_f$  vs.  $(x; y)$  and (b)  $K$  vs.  $(x; y)$  for  $X_xTa_y(TiZr)_{1-x-y}$ , with  $X=Mo$  or  $W$ , at the extreme ends of equiatomic plane.





### Partial Density of States:

We plot configurationally-averaged (element and  $l$ -decomposed  $s$ ,  $p$ , and  $d$ ) density of states for  $(\text{MoW})_{0.40}\text{Ta}_{0.20}(\text{TiZr})_{0.40}$  [C1],  $(\text{MoW})_{0.80}\text{Ta}_{0.10}(\text{TiZr})_{0.10}$  [C6], and  $(\text{MoW})_{0.80}\text{Ta}_{0.125}(\text{TiZr})_{0.075}$  [C7] in Fig. S3, and, with Al-addition in Fig. S4 for  $(\text{MoW})_{0.80}\text{Ta}_{0.05}(\text{TiZr})_{0.10}\text{Al}_{0.05}$ , which may be compared to those in main text, Fig. 2. Moving across C1-C6-C7 alloys in Fig. S3, the electron doping with increasing MoW stabilizes the alloy by filling *non-bonding*  $d$ -states of Ti/Zr, which moves Fermi energy ( $\epsilon_F$ ) into the pseudogap. However, in Fig. S4, adding 5%Al to C7 adds some hole states to the alloy and empties some non-bonding  $d$ -states of Ti/Zr, which destabilizes  $(\text{MoW})_{0.80}\text{Ta}_{0.05}(\text{TiZr})_{0.10}\text{Al}_{0.05}$ .

**Figure S3.** Partial [and  $l$ -decomposed ( $s$ ,  $p$ ,  $d$ )] density of states of each constituent of equiatomic  $(\text{MoW})_{0.40}\text{Ta}_{0.20}(\text{TiZr})_{0.40}$  (C1),  $(\text{MoW})_{0.80}\text{Ta}_{0.10}(\text{TiZr})_{0.10}$  [C6], and  $(\text{MoW})_{0.80}\text{Ta}_{0.125}(\text{TiZr})_{0.075}$  [C7]. The plot is relative to the Fermi energy [ $\epsilon_F$ ; vertical-dashed line at 0]. Increasing VEC for C6 & C7 by adding %MoW (VEC=6) energetically stabilizes the alloy by filling bonding  $d$ -states of Ti/Zr, moving  $\epsilon_F$  towards the pseudogap. Further tuning Ta (VEC=5) vs Ti/Zr (VEC=4) while keeping MoW fixed moves  $\epsilon_F$  exactly to the pseudogap, making the alloy energetically more stable than C1/C6 (see the main text, Fig.2).

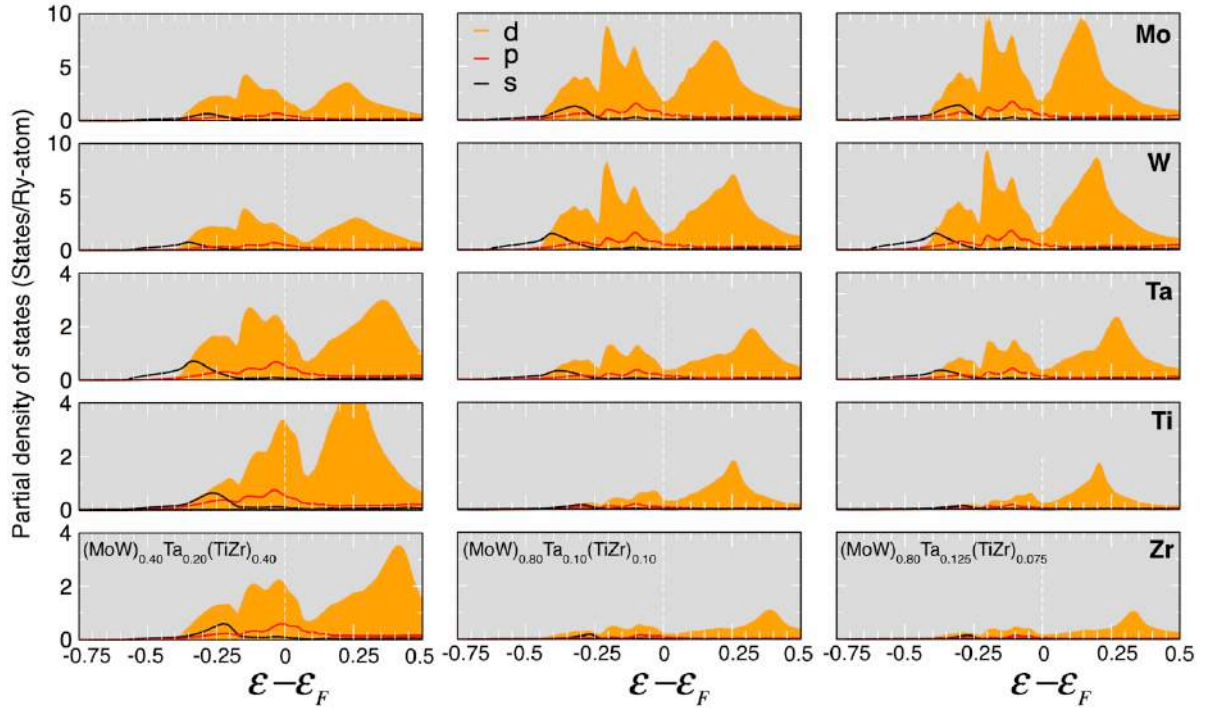
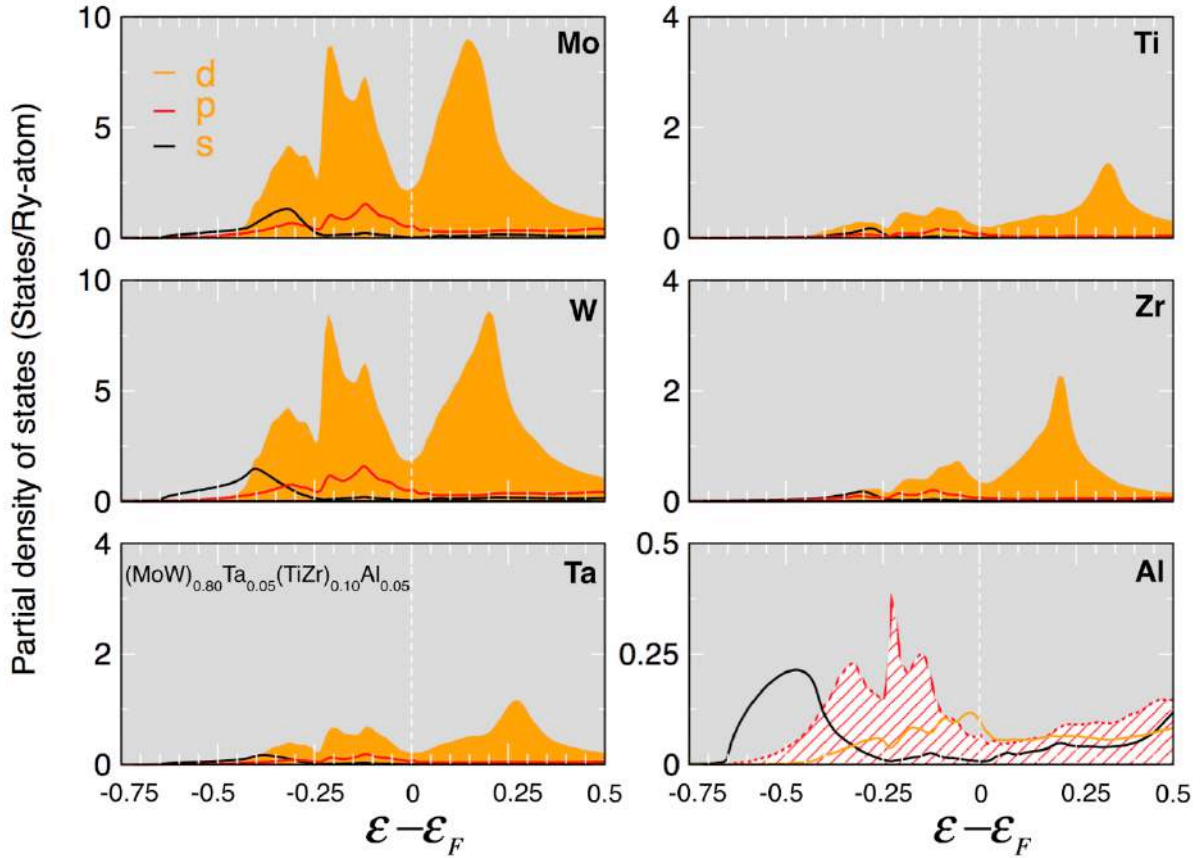


**Figure S4.** (Color online) Same as Fig. S3, except for  $(\text{MoW})_{0.80}\text{Ta}_{0.05}(\text{TiZr})_{0.10}\text{Al}_{0.05}$ . Adding Al (VEC=3) to C6 at the expense of Ta adds more hole states, which moves some non-bonding Ti/Zr  $d$ -states to  $\epsilon_F$  and destabilizes the alloys with respect to C7 alloy; this moves pseudogap region above  $\epsilon_F$ .

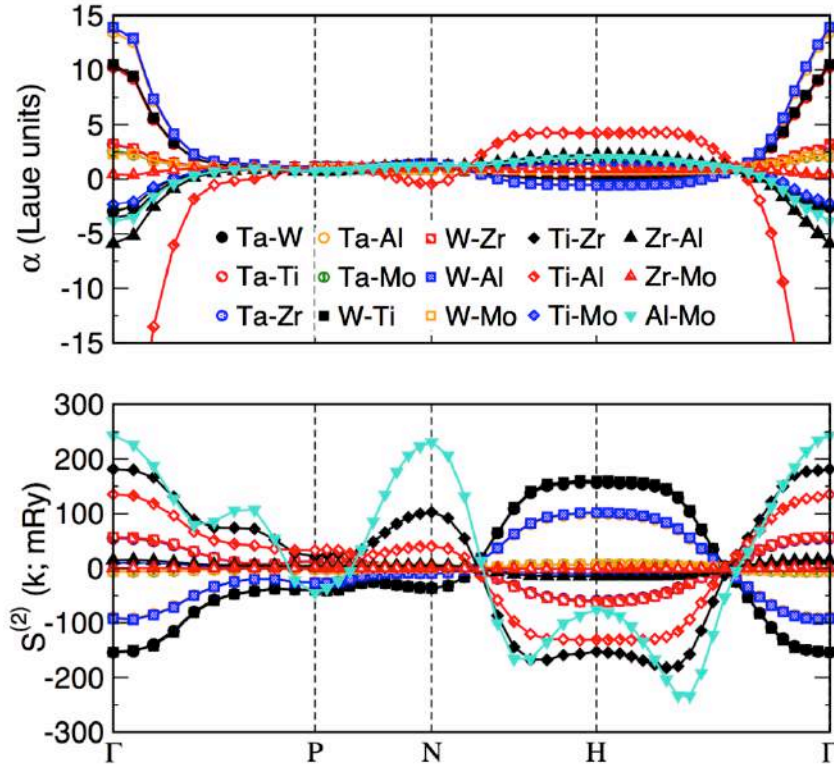


### Short-range order of $(\text{MoW})_{0.80}\text{Ta}_{0.05}(\text{TiZr})_{0.10}\text{Al}_{0.05}$ :

Besides helping with weight-reduction, aluminum doping may promote oxide-scale formation for protection of the bulk with the correct segregation properties. To assess this, we calculated the short-range order of Al-doped [C6] alloy. We show in text, Fig. 2 and discussion, that on adding 5%Al at the expense of Ta to C6 causes  $d$ -state around  $\Gamma$  at  $\epsilon_F$ . This Fermi surface feature makes  $E_f$  much more positive (+6.8 mRy), which is visible through strong clustering behavior in Fig. S5 with  $T_{sp}=780$  K. The correlations in Al-doped alloy is dominated by W-Al and W-Mo pairs, however, the clustering is driven by Al-Mo pairs in  $S^{(2)}_{\text{AlMo}}(\Gamma)$ . Clearly, adding Al at the expense of Ta or TiZr decreases VEC and drops  $\epsilon_F$  into  $d$ -states, which reduces stability. This tells us that VEC must be kept high enough such that alloy has  $E_f \sim 0$

with large bulk moduli  $K$ . This could be done by appropriately tuning %Ta and %TiZr in the alloy (Fig. 1).

**Figure S5.** We plot SRO correlations  $\alpha_{\mu\nu}$  (top) and energies  $S_{\mu\nu}$  (bottom) along high-symmetry of the BCC-BZ for  $(\text{MoW})_{0.80}\text{Ta}_{0.05}(\text{TiZr})_{0.10}\text{Al}_{0.05}$ . For Al-doped alloy, W-Al and W-Mo pairs dominate correlations, however, the clustering is driven Al-Mo pairs in  $S_{\text{AlMo}}^{(2)}(\Gamma)$  with  $T_{\text{sp}}=780$  K.

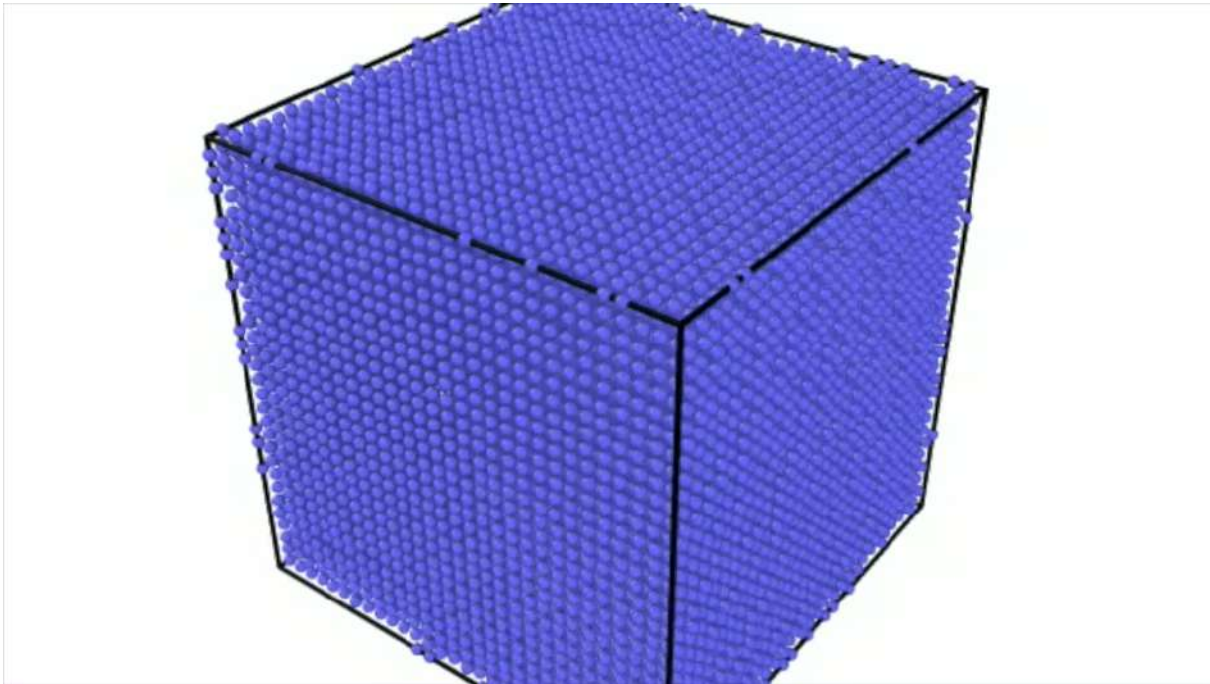


### **MD-simulations of $(\text{MoW})_{0.85}\text{Ta}_{0.10}(\text{TiZr})_{0.05}$ [C4] alloy:**

The highly-parallelized Large-scale Atomistic Molecular Massively Parallelized Simulator (LAMMPS)<sup>20</sup> package is used for all the molecular dynamics simulations (MD). The visual analysis and post-processing of molecular trajectories is performed with OVITO (the open visualization tool).<sup>21</sup> The MD simulations on MoTaWTiZr were performed after assimilating the EAM (i.e., Embedded Atom Method)<sup>22</sup> alloy potential parameters for Mo, Ta, W, Ti and Zr from the EAM database<sup>23</sup> to model the elemental cross- and self-interactions. The EAM force-field for the quinary alloy is verified against our DFT calculations for  $A2$ -phase, structural properties and elastic modulus parameters for the phase segregating regions in the design space. A deviation from KKR-CPA predictions arise only when electronic effects

become dominant in the alloy (above  $\text{MoW} > 0.85$ ) [see main text, Fig.3]. The details of the functional forms of these atomic interactions are available in the literature.<sup>22,23</sup>

**Movie S1.** (movie) Uniaxial quasi-static compression  $\langle 100 \rangle$  at 300 K for non-equiatomic  $(\text{MoW})_{0.85}\text{Ta}_{0.10}(\text{TiZr})_{0.05}$  [C4] alloy. Straining till 0.065 shows no deviation from  $A2$  (blue) coordination, beyond which instability is triggered (see main text, Fig.4(b)), which provide preferential sites for shear-band formation (white color atoms).



#### **XRD/SEM measurements on equiatomic high-entropy alloy:**

The x-ray diffraction pattern (Fig. S6 (a)) indicates presence of two (major/minor) phases. The phases were indexed as a disordered  $A2$  phase with  $Im-3m$  space group, and a minor phase of  $Fd(-3)m$  space group. The  $A2$  lattice parameter was measured as 3.1713 Å (std. dev: 0.0002 Å). Figure. S6 (b) shows the SEM micrograph of the alloy with a two-phase alloy evident. The compositions are summarized in Table S1. The major phase ( $A2$ ) is Mo, W and Ta rich, with small amounts of Ti and Zr incorporated in it. Given the higher melting temperatures of Mo, W and Ta, the major phase is likely to be the primary solidifying phase during the final step of casting. As this phase forms during casting, Ti and Zr are rejected into the surrounding liquid, which subsequently freezes. Hence, the minor phase is Ti and Zr rich

and incorporates small amounts of the refractory metals. For a preliminary assessment of mechanical behavior of the alloy, thirty nanoindentation measurements were made on the major phase, although there still may be a small effect from the minor phase. The contact depth in the nanoindentation measurements were ~200nm. The size of the phase features, as seen in the microstructure of Fig. S6 (b) is significantly larger than the nanoindentation (and expected interaction volumes).

**Figure S6.** (a) X-Ray diffraction pattern from the equiatomic alloy; (b) Backscattered SEM of the equiatomic alloy – the brighter contrast is the (Mo,W,Ta)-based solid solution, while the darker phase is the (Ti,Zr)-rich phase. The scale bar is 300  $\mu\text{m}$ .

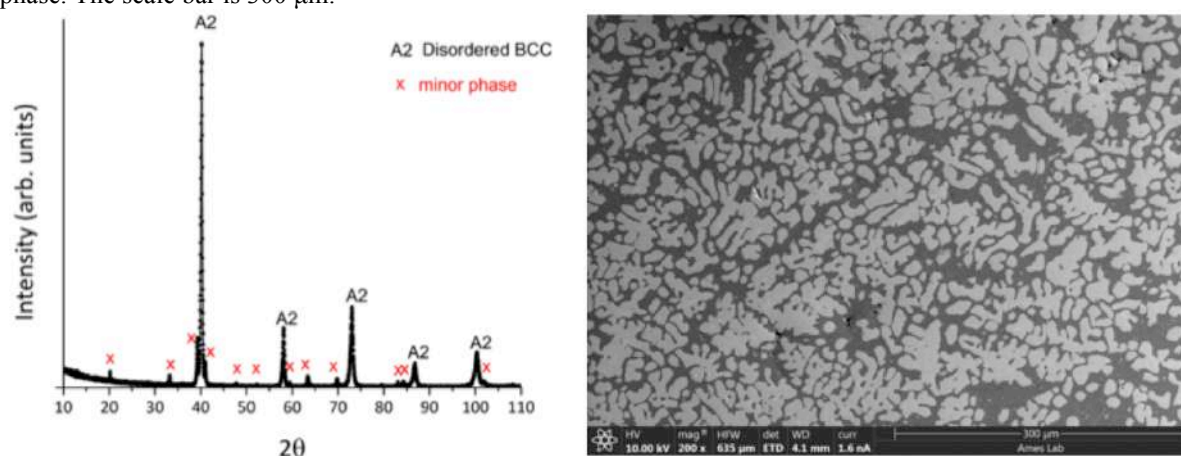


**Table S1.** Table Caption: Phase compositions, as determined using EDS. Compositions are provided in at.%. Standard deviations are provided in parentheses.

	Mo	W	Ta	Ti	Zr
major phase [ <i>Im</i> $\bar{3}$ <i>m</i> ]	22.96(1.79)	33.63(2.57)	28.31(0.44)	11.19(1.79)	3.90 (0.52)
minor phase [ <i>Fd</i> (-3) <i>m</i> ]	8.44 (0.82)	0.89(0.15)	3.06(0.22)	32.61(0.35)	55.00 (0.87)



## Reference:

- [1] J. Koringa, *Physica* **1947**, *13*, 392.
- [2] W. Kohn, N. Rostoker, *Phys. Rev.* **1954**, *94*, 1111.
- [3] B. Velický, S. Kirkpatrick, H. Ehrenreich, *Phys. Rev.* **1968**, *175*, 747.
- [4] G.M. Stocks, W.N. Temmerman, B.L. Gyorffy, *Phys. Rev. Lett.* **1978**, *41*, 339.
- [5] D.D. Johnson, A.V. Smirnov, S.N. Khan, *MECCA: Multiple-scattering Electronic-structure Calculations for Complex Alloys* (KKR-CPA Program, ver. 2.0), Iowa State University and Ames Laboratory, 2015.
- [6] P. Singh, A.V. Smirnov, D.D. Johnson, *Phys. Rev. B* **2015**, *91*, 224204.
- [7] A. Sharma, P. Singh, P.K. Liaw, D.D. Johnson, G. Balasubramanian, *Sci. Rep.* **2016**, *6*, 31028.
- [8] G. Kresse, J. Hafner, *Phys. Rev. B* **1993**, *47*, 558; *ibid.* **1994**, *49*, 14251.
- [9] A. Gulans *et al.*, *J. of Phys.: Cond. Matter* **2014**, *26*, 363202.
- [10] S. Curtarolo, G.L.W. Hart, M.B. Nardelli, N. Mingo, S. Sanvito, O. Levy, *Nat Mater* **2013**, *12* (3), 191.
- [11] S. Curtarolo, D. Morgan, K. Persson, J. Rodgers, and G. Ceder, *Phys. Rev. Lett.* **2003**, *91*, 135503.
- [12] W. Setyawan, S. Curtarolo, *Comp. Mater. Sci.* **2010**, *49*, 299.
- [13] Jain, A. *et al.*, *Comp. Mater. Sci.* **2011**, *50*, 2295.
- [14] S. Wang, Z. Wang, W. Setyawan, N. Mingo, S. Curtarolo, *Phys. Rev. X* **2011**, *1*, 021012.
- [15] H. Koinuma, I. Takeuchi, *Nat Mater* **2004**, *3*, 429.
- [16] J.L. Spivack *et al.*, *Appl. Catal. A* **2003**, *254*, 5.
- [17] J. S. Dugdale and D. K. C. MacDonald, *Phys. Rev.* **1953**, *89*, 832.
- [18] T. M. Pollock, *Nat. Mater.* **2016**, *15*, 809.
- [19] G. Liu, G.J. Zhang, F. Jiang, X.D. Ding, Y. J. Sun, J. Sun, E. Ma, *Nat. Mater.* **2013**, *12*, 344.
- [20] S. Plimpton, *J. of Comp. Phys.* **1995**, *117*, 1.
- [21] A. Stukowski, *Modelling and Simulation in Materials Science and Engineering*, 18 (2010).
- [22] M.S. Daw, M.I. Baskes, *Phys. Rev. B* **1984**, *29*, 6443.
- [23] X.W. Zhou, R.A. Johnson, H.N.G. Wadley, *Phys. Rev. B* **2004**, *69*, 1.